

# BI-GCN: Boundary-Aware Input-Dependent Graph Convolution Network for Biomedical Image Segmentation

Yanda Meng<sup>1</sup>

Hongrun Zhang<sup>1</sup>

Dongxu Gao<sup>2</sup>

Yitian Zhao<sup>3</sup>

Xiaoyun Yang<sup>4</sup>

Xuesheng Qian<sup>5</sup>

Xiaowei Huang<sup>6</sup>

Yalin Zheng<sup>\*1</sup>

yalin.zheng@liverpool.ac.uk

<sup>1</sup> Department of Eye and Vision Science, University of Liverpool, Liverpool, UK.

<sup>2</sup> School of Computing, University of Portsmouth, Portsmouth, UK.

<sup>3</sup> Cixi Institute of Biomedical Engineering, Chinese Academy of Sciences, Ningbo, China.

<sup>4</sup> Remark AI UK Limited, London, United Kingdom.

<sup>5</sup> China Science IntelliCloud Technology Co., Ltd, Shanghai, China.

<sup>6</sup> Department of Computer Science, University of Liverpool, Liverpool, UK.

## Abstract

Segmentation is an essential operation of image processing. The convolution operation suffers from a limited receptive field, while global modelling is fundamental to segmentation tasks. In this paper, we apply graph convolution into the segmentation task and propose an improved *Laplacian*. Different from existing methods, our *Laplacian* is data-dependent, and we introduce two attention diagonal matrices to learn a better vertex relationship. In addition, it takes advantage of both region and boundary information when performing graph-based information propagation. Specifically, we model and reason about the boundary-aware region-wise correlations of different classes through learning graph representations, which is capable of manipulating long range semantic reasoning across various regions with the spatial enhancement along the object's boundary. Our model is well-suited to obtain global semantic region information while also accommodates local spatial boundary characteristics simultaneously. Experiments on two types of challenging datasets demonstrate that our method outperforms the state-of-the-art approaches on the segmentation of polyps in colonoscopy images and of the optic disc and optic cup in colour fundus images.

# 1 Introduction

Accurate examination of anatomical structures in biomedical images helps clinicians determine the likelihood of many medical conditions and diseases. For example, shapes of the optic disc (OD) and optic cup (OC) of the retina are essential in the diagnosis of glaucoma, a chronic degenerative disease that causes irreversible loss of vision [60]. Likewise, colorectal polyps are linked with an increased risk of having colorectal cancer, the third most common cancer worldwide [28]. However, it is impractical to manually annotate these structures in clinics due to the time-consuming, labour-intensive, and error-prone process. Automated and accurate image segmentation is increasingly needed.

Deep learning-based pixel-wise biomedical image segmentation methods, such as [4, 10, 27, 34, 38, 41], are popular because of Convolutional Neural Network’s (CNN’s) excellent ability to extract and reason about semantic features, and correlations among different classes. *Fan et al.* [8] and *Zhang et al.* [38] studied the correlations between the foreground and background classes using a similar foreground erasing mechanism, which achieved state-of-the-art performance in the colonoscopy polyps segmentation tasks. Due to limited receptive fields of CNN, they incorporated dense dilation [35] convolutions to enlarge the receptive regions for long range context reasoning. Along the same line, *Fu et al.* [10] proposed multiscale input and side-output mechanism with deep supervision, which achieves multi-level receptive field fusion for long range relationship aggregation. However, this is inefficient since stacking local cues cannot always precisely handle long range context relationships. Especially for pixel-level classification problems, such as segmentation, performing long range interactions is an important factor for reasoning in complex scenarios [9]. For example, it is prone to assign visually similar pixels in a local region into the same category. Meanwhile, pixels of the same object but distributed in a distance are difficult to construct dependencies. Recent graph propagation-based reasoning approaches [6, 20, 37] that use *Laplacian* smoothing-based graph convolution [17], provide specific benefits in the sense of global long range information reasoning. They estimated the initial graph structure from a data-independent *Laplacian* matrix defined by randomly initialized adjacency matrix [6, 37] or hand-crafted adjacency matrix [17, 20]. However, one may make a model to learn a specific long range context pattern [38], which is less related to the input features. Differently, as seen in previous works, the graph structure can be estimated with the similarity matrix from the input data [19], we estimate the initial adjacency matrix in a data-dependent way. Specifically, we implement two diagonal matrices to perform channel-wise attention on the dot product distance of input vertex embeddings, and measure spatial-wise weighted relations among different vertices. In this way, our model is capable of learning an input-related long range context pattern, which improves the model segmentation performance, please read *Ablation Study* (Section 3.4) for more details.

Different to the dense pixel classification, recent polygon-based methods [21, 22] explored the spatial features of an object’s boundary. They regressed the predefined vertex position along the object borders then linked the predicted vertices to form a polygon to indicate the object’s boundary. For example, *Meng et al.* proposed a CNN and Graph Convolution Network (GCN) aggregated network [21] to directly regress the vertices’ coordinates of the OC and OD boundaries. It is well established that boundary knowledge is essential in obtaining spatial features in segmentation tasks. With regard to biomedical image segmentation, the boundary accuracy is often more critical than that of the regional pixel-wise coverage [22]. In this work, we explicitly exploit the boundary information to fuse the boundary features into the proposed graph convolution, proposing a boundary-aware graph convolution.

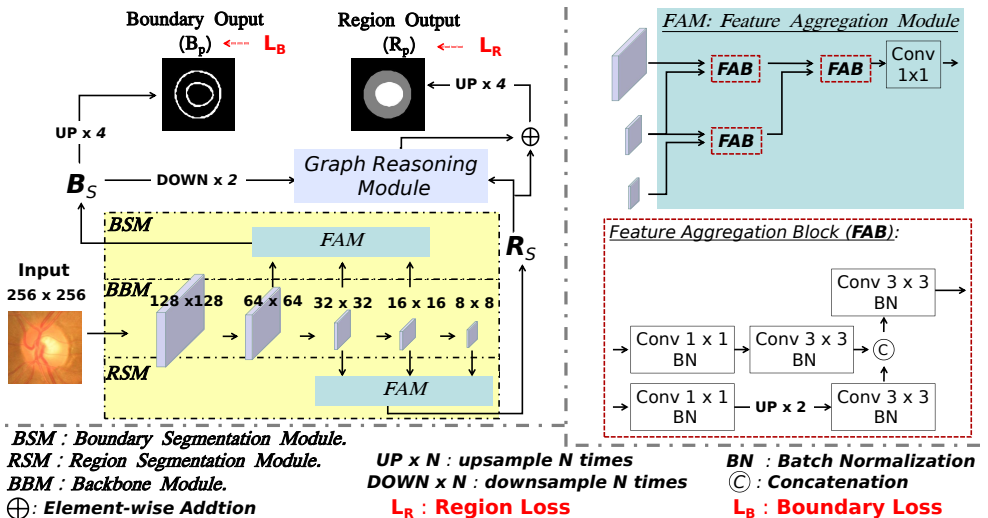


Figure 1: Overview of the proposed graph-based segmentation network (left), Feature Aggregation Module (right). Upsample and downsample layers are implemented through learnable bilinear interpolation.

Our experimental results prove that the proposed boundary-aware graph convolution can improve the region segmentation performance. Along the same line, recent methods, such as [9, 23, 25, 33, 39], considered object’s boundary segmentation while tackling object region segmentation tasks. However, they treated it as a multi-task learning problem, leaving the model to learn a robust backbone. Differently, we explicitly fuse the boundary information to improve the classic graph convolution’s performance on the segmentation task.

This work proposes a novel GCN that reasons the boundary-aware region-wise correlations of different classes through learning graph representations. Specifically, with an input image, multi-level features were learned through a Backbone Module. Further, we constructed two feature aggregation modules upon shallow- and deep-level backbone features respectively for boundary and region characteristics learning, namely Boundary Segmentation Module (BSM) and Region Segmentation Module (RSM). The outputs of BSM and RSM were fed into the proposed graph reasoning module GRM for long range feature reasoning. In detail, the region-wise output ( $R_S$ ) from RSM and the boundary-wise output ( $B_S$ ) from BSM were embedded into graph representation in terms of vertex embeddings. Within the GRM, we proposed a new Boundary-aware Input-dependent Graph Convolution (BI-GConv). Specifically, the input-dependent adjacency matrix was estimated from the input features of vertex embeddings that were refined by spatial and channel attentions. Additionally, the object’s boundary features were fused into the constructed Laplacian matrix  $\tilde{L}$ , enhancing the characteristics along the boundaries to emphasize the boundary-aware correlations across different regions. Our experimental results show that the proposed framework makes a large improvement over state-of-the-art approaches.

## 2 Method

There are four major components in the proposed model: a backbone module, a region segmentation module (*RSM*), a boundary segmentation module (*BSM*), and a graph reasoning module (*GRM*). Fig. 1 provides an overview of the model architecture and Fig. 2 highlights the proposed *GRM* and *BI-GConv*. Given an input image, we extract its multi-level features through a backbone module. Following the previous PraNet [8], we adopt the truncated Res2Net [12] as backbone module due to its superior ability to extract discriminative features in segmentation tasks.

**Feature Aggregation.** For the *RSM* and *BSM*, we applied two feature aggregation modules to different levels of features of the backbone to extract full spectrum of semantic and spatial characteristics. As observed by previous studies [36, 40], deep- and shallow-layer features from different levels complement each other, where the deep-layer features contain rich semantic region information while the shallow-layer features preserve the sufficient spatial boundary information. Thus, we applied feature aggregation module on relative deep-level and low-level features for *BSM* and *RSM* respectively. In detail, the feature aggregation module contains several feature aggregation blocks to fuse low-to-high level features hierarchically and iteratively. Notably, in the feature aggregation block, two  $1 \times 1$  convolutions are applied on two resolution’s features respectively to reduce and maintain the same channel size. After feature aggregation module, the output  $B_s$  and  $R_s$  have sizes of  $64 \times 64 \times l$  and  $32 \times 32 \times 2$ , respectively. We downsampled  $B_s$  by 2 and fed it into the *GRM* together with  $R_s$ . Downsample is for maintaining the same feature map size and reducing the computational overhead.

**Classic Graph Convolution.** We first revisit the classic graph convolution. Given a graph  $G = (V, E)$ , normalized *Laplacian* matrix is  $L = I - D^{-\frac{1}{2}}AD^{-\frac{1}{2}}$ , where  $I$  is the identity matrix,  $A$  is the adjacency matrix, and  $D$  is a diagonal matrix that represents the degree of each vertex in  $V$ , such that  $D_{ii} = \sum_j A_{i,j}$ . The *Laplacian* of the graph is a symmetric and positive semi-definite matrix, so  $L$  can be diagonalized by the Fourier basis  $U \in \mathbb{R}^{N \times N}$ , such that  $L = U\Lambda U^T$ . Thus, the spectral graph convolution of  $i$  and  $j$  can be defined as  $i * j = U((U^T i) \odot (U^T j))$  in the Fourier space. The columns of  $U$  are the orthogonal eigenvectors  $U = [u_1, \dots, u_n]$ , and  $\Lambda = \text{diag}([\lambda_1, \dots, \lambda_n]) \in \mathbb{R}^{N \times N}$  is a diagonal matrix with non-negative eigenvalues. Since  $U$  is not a sparse matrix, this operation is computationally expensive. Defferrard et al. [7] proposed that the convolution operation on a graph can be defined by formulating spectral filtering with a kernel  $g_\theta$  using a recursive Chebyshev polynomial in Fourier space. The filter  $g_\theta$  is parameterized as a Chebyshev polynomial expansion of order  $K$ , such that  $g_\theta(L) = \sum_k \theta_k T_k(\hat{L})$ , where  $\theta \in \mathbb{R}^K$  is a vector of Chebyshev coefficients, and  $\hat{L} = 2L/\lambda_{\max} - I_N$  represents the rescaled *Laplacian*.  $T_k \in \mathbb{R}^{N \times N}$  is the Chebyshev polynomial of order  $K$ . In [10], Kipf et al. further simplified the graph convolution as  $g_\theta = \theta(\hat{D}^{-\frac{1}{2}}\hat{A}\hat{D}^{-\frac{1}{2}})$ , where  $\hat{A} = A + I$ ,  $\hat{D}_{ii} = \sum_j \hat{A}_{ij}$ , and  $\theta$  is the only Chebyshev coefficient left. The corresponding graph *Laplacian* adjacency matrix  $\hat{A}$  is hand-crafted, which leads the model to learn a specific long range context pattern rather than the input-related one [18]. Thus, we refer to the classic graph convolution as input-independent graph convolution.

**Boundary-Aware Input-dependent Graph Convolution (*BI-GConv*).** Given the input region features  $R_s \in \mathbb{R}^{N \times C}$ , where  $C$  is the channel size;  $N = H \times W$  is the number of spatial locations of input feature, which is referred to as the number of vertexes. Firstly, we construct the input-dependent adjacency matrix. In detail, we implement two diagonal matrices ( $\tilde{\Lambda}^e$  and  $\tilde{\Lambda}^s$ ) to perform channel-wise attention on the dot-product distance of input

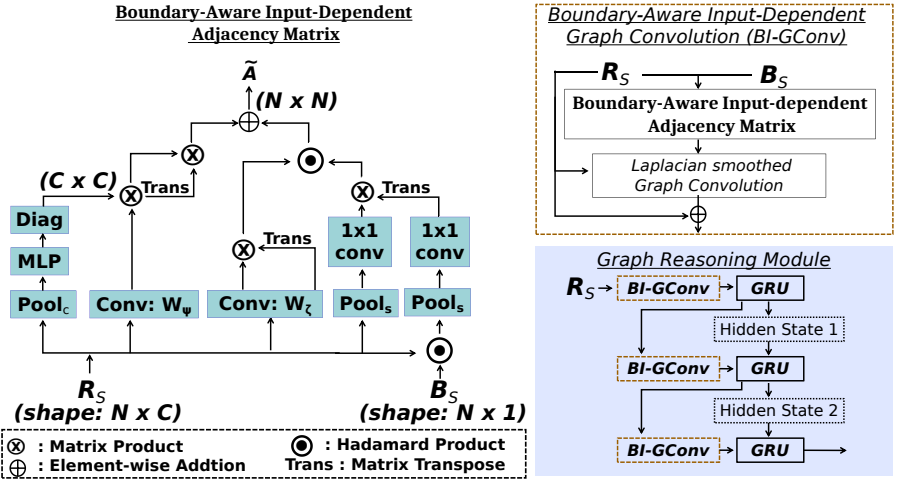


Figure 2: Overview of the newly proposed Boundary-Aware Input-Dependent Adjacency Matrix, *BI-GConv* and *GRM*.

vertex embeddings, and measure spatial-wise weighted relations among different vertices, respectively. For example,  $\tilde{\Lambda}^c(R_s) \in \mathbb{R}^{C \times C}$  is the diagonal matrix that contains channel-wise attention on the dot-product distance of the input vertex embeddings;  $\tilde{\Lambda}^s(R_s) \in \mathbb{R}^{N \times N}$  is the spatial-wise weighted matrix, measuring the relationships among different vertices.

$$\tilde{\Lambda}^c(R_s) = \text{diag}\left(MLP(Pool_c(R_s))\right), \quad (1)$$

where  $Pool_c(\cdot)$  denotes the global max pooling for each vertex embedding;  $MLP(\cdot)$  is a multi-layer perceptron with one hidden layer. On the other hand,

$$\tilde{\Lambda}^s(R_s) = \text{diag}\left(Conv(Pool_s(R_s))\right), \quad (2)$$

where  $Pool_s(\cdot)$  represents the global max pooling for each position in the vertex embedding along the channel axis;  $Conv(\cdot)$  is a  $1 \times 1$  convolution layer. The data-dependent adjacency matrix  $\tilde{A}$  is given by spatial and channel attention-enhanced input vertex embeddings. We initialize the input-dependent adjacency matrix  $\tilde{A}$  as:

$$\tilde{A} = \psi(R_s, W_\psi) \cdot \tilde{\Lambda}^c(R_s) \cdot \psi(R_s, W_\psi)^T + \phi(R_s, W_\phi) \cdot \phi(R_s, W_\phi)^T \odot \tilde{\Lambda}^s(R_s), \quad (3)$$

where  $\cdot$  represents matrix product;  $\odot$  denotes Hadamard product;  $\psi(R_s, W_\psi) \in \mathbb{R}^{N \times C}$  and  $\phi(R_s, W_\phi) \in \mathbb{R}^{N \times C}$  are both linear embeddings ( $1 \times 1$  convolution);  $W_\psi$  and  $W_\phi$  are learnable parameters.

Secondly, we fuse the boundary information through integrating the predicted boundary function map  $B_s \in \mathbb{R}^{N \times 1}$  into the built *Laplacian* matrix  $\tilde{L}$ , which allows us to leverage the spatial hint of the object's boundary. Specifically, we fuse it into the spatial-wise weighted matrix  $\tilde{\Lambda}^s(R_s)$ . The boundary-aware spatial weighted matrix  $\tilde{\Lambda}_b^s(R_s, B_s)$  is given as follows:

$$\tilde{\Lambda}_b^s(R_s, B_s) = Conv\left(Pool_s(R_s)\right) \cdot \left(Conv\left(Pool_s(R_s \odot B_s)\right)\right)^T \quad (4)$$

where  $\odot$  is the broadcasting Hadamard product along channels;  $Conv(\cdot)$  is a  $1 \times 1$  convolution layer. In this way, the features of boundary pixels are emphasized by assigning larger weights. As this is the case, the proposed boundary-aware graph convolution can take the spatial characteristics of the boundary into account when reasoning the correlations between different regions. Then, the boundary-aware input-dependent adjacency matrix  $\tilde{A}$  will be given as:

$$\tilde{A} = \psi(R_s, W_\psi) \cdot \tilde{\Lambda}^c(R_s) \cdot \psi(R_s, W_\psi)^T + \zeta(R_s, W_\zeta) \cdot \zeta(R_s, W_\zeta)^T \odot \tilde{\Lambda}_b^s(R_s, B_s), \quad (5)$$

where  $\zeta(R_s, W_\zeta) \in \mathbb{R}^{N \times C}$  is  $1 \times 1$  convolution;  $W_\zeta$  is learnable parameter. Fig. 2 shows a detailed demonstration of  $\tilde{A}$ . With the constructed  $\tilde{A}$ , the normalized *Laplacian* matrix is given as  $\tilde{L} = I - \tilde{D}^{-\frac{1}{2}} \tilde{A} \tilde{D}^{-\frac{1}{2}}$ , where  $I$  is the identity matrix,  $\tilde{D}$  is a diagonal matrix that represents the degree of each vertex, such that  $\tilde{D}_{ii} = \sum_j \tilde{A}_{i,j}$ . Inspired by [18], in order to reduce the complexity ( $\mathcal{O}(N^2)$ ) of calculating *Laplacian* matrix  $\tilde{L}$ , we calculate the degree matrix  $\tilde{D}$  as:

$$\tilde{D} = \text{diag}\left(\psi\left(\tilde{\Lambda}^c(\psi^T \cdot \vec{1})\right)\right) + \text{diag}\left(\zeta(\zeta^T \cdot \vec{1})\right) \odot \tilde{\Lambda}_b^s, \quad (6)$$

where  $\vec{1}$  denotes all-one vector in  $\mathbb{R}^N$ , and the calculation in the inner bracket is executed first. By doing this, we can override the quadratic order of computation, thus reduce the computational overhead. Given computed  $\tilde{L}$ , with  $R_s$  as the input vertex embeddings, we formulate the single-layer *BI-GConv* as :

$$Y = \sigma(\tilde{L} \cdot R_s \cdot W_G) + R_s, \quad (7)$$

where  $W_G \in \mathbb{R}^{C \times C}$  denotes the trainable weights of the *BI-GConv*;  $\sigma$  is the ReLu activation function;  $Y$  is the output vertex features. Moreover, we add a residual connection to reserve the features of input vertices.

**Graph Reasoning Module.** We build the *GRM* with the chained *BI-GConv* layers in order to focus on the long-term dependency between chained graph layers. Fig. 2 shows an overview of the proposed *GRM* with three *BI-GConv* layers of Gated Recurrent Unit (*GRU*) [2] connection, which gains the best performance. Please note, these layers can also be connected by *Residual* [3] connections; comprehensive comparison results of these two connection manners can be found in the supplementary material.

## 3 Experiments

### 3.1 Datasets

We use a retinal and a colorectal dataset, each of them is merged from five different datasets of its kind. The details of boundary ground truth generation can be found in the supplementary material.

**Fundus OD and OC images:** 2,068 images from five datasets (Refuge [26], Drishti-GS [29], ORIGA [40], RIGA [4], RIM-ONE [41]) are pooled together. 613 images are randomly selected for test and the remaining 1,455 are for training and validation. We follow [41] to crop a subimage of  $256 \times 256$  pixels centered at the OD center for the subsequent analysis. The training and test data come from the same data source (**seen data**), OD and OC segmentation is used for evaluate the model’s learning ability.

**Colonoscopy polyp images:** 2,247 colonoscopy images from five datasets (ETIS [28], CVC-ClinicDB [9], CVC-ColonDB [60], EndoScene-CVC300 [62], and Kvasir [15]). All the images are resized to  $256 \times 256$  pixels. As suggested by [8], *i.e.*, 1,450 images from Kvasir [15] and CVC-ClinicDB [9] are selected as the training and validation datasets and the other 635 images from ETIS [28], CVC-ColonDB [60], EndoScene-CVC300 [62] are pooled together for independent testing (**unseen data**). By doing this, the training and test data are from different data source so as to evaluate the model’s generalization capability.

## 3.2 Implement Details and Evaluation Metrics

**Implement Details** To augment the dataset, we randomly rotate and horizontally flip the training dataset with the probability of 0.3. The rotation ranges from  $-30$  to  $30$  degree. 10% of the training dataset are randomly selected as the validation dataset. The network is trained end-to-end by Adam optimizer [16] for 50 thousands iterations, with a learning rate of  $6e-3$  and decayed to  $0.36e-3$  after 30 thousand iterations. The batch size is set at 48. All the training processes are performed on a server with four TESLA V100, and all the test experiments are conducted on a local workstation with *Intel(R) Xeon(R) W-2104 CPU* and *Geforce RTX 2080Ti GPU*. **Code is available at:** <https://github.com/smallmax00/BI-GConv>

**Loss Function.** The overall loss function is defined as:  $L_{total} = L_R + \alpha \cdot L_B$ , where  $\alpha$  balances the losses between region and boundary predictions; a detailed ablation study on  $\alpha$  is presented in the supplementary material. We adopt standard Dice Loss [24] for the region ( $L_R$ ) and boundary ( $L_B$ ) segmentation supervision.

**Evaluation Metrics.** Typical region segmentation metrics such as Dice similarity score (*Dice*) and balanced accuracy (*B-Acc*) are applied, where *B-Acc* is the mean value of *Sensitivity* and *Specificity*. Boundary Intersection-over-Union (*BIOU*) [9] is used as the boundary segmentation measurement. Details of the utilization of *BIOU* can be found in the supplementary material. To show statistical significance, 95% confidence interval is generated by using 2000 sample bootstrapping for all the evaluation metrics.

## 3.3 Results

We show qualitative (Fig. 3) and quantitative results (Tab. 1, Tab. 2) of the polyps, and OC and OD segmentation tasks. More qualitative results can be found in the supplementary materials. We compared the proposed method with two classic models (*i.e.* *U-Net* [27], *U-Net++* [40]) and five cutting-edge models, such as *M-Net* [10], *RBA-Net* [20], *PsiNet* [25], *PraNet* [8] and *ACSNet* [33] for OC and OD and polyps segmentation. Notably, we sampled 360 vertices for *RBA-Net* [20] to construct a smooth boundary. *M-Net* [10] is specially designed for OC and OD segmentation task.

**Learning Ability.** We conduct experiments to validate our model’s learning ability on *seen* data (*i.e.* OC and OD segmentation datasets). As shown in Tab. 1, we achieved 88.8 % and 97.7 % *Dice* scores on OC and OD segmentation respectively, which outperforms region segmentation based approaches *U-Net* [27], *U-Net++* [40], *PraNet* [8] and *M-Net* [10] by 3.5 %, 3.1 %, 2.9 % and 1.9 % respectively, boundary regression approach *RBA-Net* [20] by 1.9 %, and region-boundary hybrid approach *PsiNet* [25] by 2.8 %.

**Generalization Capability.** We conduct experiments to test the model’s generalizability on *unseen* data (*i.e.* polyps segmentation datasets). The three unseen datasets each have their own set of challenges and characteristics. For example, CVC-ColonDB [60] is a small-scale

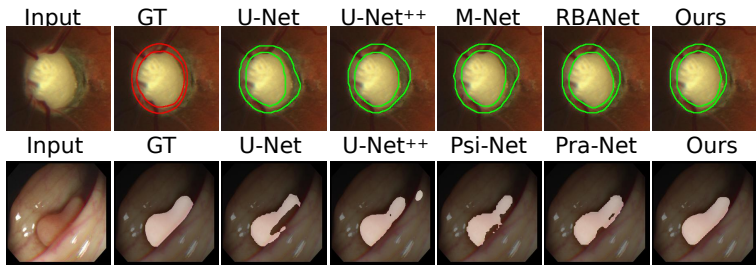


Figure 3: Visualization of OC and OD segmentation (first row), where the boundary of region segmentation predictions are extracted and plotted on the input image for better visualization. Second row shows the colonoscopy polyp segmentation comparisons. Our proposed method consistently produces segmentation results closest to the ground truth.

Table 1: Quantitative segmentation results of OC and OD and polyps on respective testing datasets. The performance is reported as *Dice* (%), *B-Acc* (%), *BloU* (%). 95 % confidence intervals are presented in the brackets, respectively.

Methods	OC			OD			Polyps		
	<i>Dice</i> (%) $\uparrow$	<i>B-Acc</i> (%) $\uparrow$	<i>BloU</i> (%) $\uparrow$	<i>Dice</i> (%) $\uparrow$	<i>B-Acc</i> (%) $\uparrow$	<i>BloU</i> (%) $\uparrow$	<i>Dice</i> (%) $\uparrow$	<i>B-Acc</i> (%) $\uparrow$	<i>BloU</i> (%) $\uparrow$
<i>U-Net</i> [14]	85.3 (84.0, 85.9)	88.1 (86.8, 88.9)	80.1 (78.7, 81.5)	95.0 (94.0, 96.2)	96.0 (95.1, 96.7)	86.2 (85.1, 87.3)	67.7 (63.6, 70.1)	80.7 (77.0, 84.9)	61.0 (58.6, 64.1)
<i>U-Net++</i> [15]	86.0 (84.7, 87.6)	89.6 (88.3, 89.9)	81.4 (79.5, 83.0)	95.0 (93.9, 96.1)	95.9 (95.0, 96.5)	87.0 (86.3, 87.8)	67.6 (64.1, 71.0)	81.6 (76.4, 85.5)	62.1 (59.7, 64.7)
<i>M-Net</i> [16]	86.9 (86.1, 87.2)	91.7 (91.3, 92.4)	82.9 (79.5, 84.1)	96.2 (95.8, 96.6)	97.2 (96.3, 97.9)	88.1 (87.0, 88.7)	-	-	-
<i>RBA-Net</i> [17]	87.1 (86.2, 88.0)	92.5 (91.1, 92.9)	82.8 (81.6, 83.9)	96.1 (95.5, 96.7)	97.5 (96.8, 98.2)	88.9 (87.9, 89.4)	69.5 (67.2, 71.1)	84.1 (83.6, 84.7)	63.2 (60.8, 65.1)
<i>Psi-Net</i> [18]	85.7 (84.3, 86.4)	88.1 (87.5, 88.6)	80.1 (80.7, 81.0)	95.8 (94.5, 96.1)	96.7 (95.5, 97.0)	87.9 (86.4, 88.5)	67.8 (64.7, 69.9)	84.5 (81.1, 87.2)	61.1 (59.7, 63.2)
<i>ACSNet</i> [19]	85.5 (84.1, 86.7)	88.8 (88.1, 89.2)	81.1 (79.4, 82.6)	95.9 (94.5, 97.1)	96.4 (96.0, 96.7)	87.0 (85.9, 88.3)	69.1 (66.7, 71.4)	83.6 (79.7, 85.5)	65.2 (62.5, 67.7)
<i>PraNet</i> [8]	85.8 (84.5, 86.3)	88.9 (88.1, 89.2)	81.5 (80.1, 82.7)	95.5 (93.7, 97.3)	97.1 (96.2, 97.9)	86.8 (85.1, 87.7)	70.5 (68.6, 71.7)	85.6 (83.8, 86.9)	64.0 (61.6, 66.9)
<i>Ours</i>	<b>88.8</b> (88.1, 89.4)	<b>94.7</b> (94.2, 95.1)	<b>85.1</b> (83.3, 86.8)	<b>97.7</b> (97.6, 97.8)	<b>98.4</b> (98.4, 98.5)	<b>91.1</b> (90.2, 92.0)	<b>72.7</b> (70.1, 75.4)	<b>87.5</b> (86.2, 88.8)	<b>67.4</b> (65.7, 70.1)

database comprised of 15 short colonoscopy sequences. ETIS [28] is an early established dataset for colorectal cancer early diagnosis. EndoScene-CVC300 [32] is a re-annotated benchmark with associated polyp and background (mucosa and lumen). In Tab. 1, our model achieves 72.7 % *Dice* score, which outperforms the cutting-edge polyps segmentation methods *PraNet* [8] and *ACSNet* [19] by 3.1 % and 5.2 %, respectively.

**Computational Efficiency.** Tab. 2 presents the number of parameters ( $M$ ) and floating-point operations ( $FLOPs$ ) of the compared models. *Ours* and *PraNet* [8] adopt the same backbone network, thus have similar model size ( $Params$ ). However, our model iteratively and hierarchically fuse and aggregate deep- and shallow-layers features, which consume more computations. A trade-off between segmentation accuracy and computational efficiency can be determined by different number of chained *BI-GConv* layers. For example, *Ours* contains 26.6  $M$  parameters when there is one layer of *BI-GConv* in the proposed *GRM*.



Table 2: Number of parameters and FLOPs on a  $256 \times 256$  input image.

	<i>U-net</i> [10]	<i>U-Net++</i> [11]	<i>M-net</i> [12]	<i>RBA-Net</i> [13]	<i>Psi-Net</i> [14]	<i>ACSnet</i> [15]	<i>PraNet</i> [8]	<i>Ours</i>
Params (M)	17.3	36.6	10.3	34.3	7.8	29.5	30.5	32.9
FLOPs (G)	40.2	138.6	17.5	130.3	32.6	11.5	6.9	12.0

### 3.4 Ablation Study

We conducted extensive ablation studies, and all the results consolidated our model’s effectiveness. For example, the ablation results on different graph convolutions and model components are shown in Tab. 3 and Tab. 4. In the supplementary material, we report the ablation study experimental results related to the *GRM*, such as number ( $N$ ) of *BI-GConv* layers, different multi-layers connection manners (*GRU* [9] or *Residual* [13]).

Table 3: Ablation study on different graph convolutions. The performance is reported as *Dice (%)* and *BloU (%)*. 95 % confidence intervals are presented in the brackets, respectively.

Methods	OC		OD		Polyps	
	<i>Dice (%)</i> †	<i>BloU (%)</i> †	<i>Dice (%)</i> †	<i>BloU (%)</i> †	<i>Dice (%)</i> †	<i>BloU (%)</i> †
<i>Classic Graph Convolution</i> [10]	86.5	81.1	95.5	86.4	69.5	63.8
	(85.5, 87.3)	(79.9, 82.2)	(95.0, 96.1)	(85.3, 87.3)	(66.9, 71.6)	(61.1, 66.0)
<i>Dependent (channel)</i>	87.3	83.0	95.9	86.8	69.9	64.0
	(86.5, 87.9)	(81.2, 85.2)	(95.2, 96.5)	(85.7, 87.4)	(67.2, 71.9)	(61.1, 66.7)
<i>Dependent (spatial)</i>	87.8	83.5	96.1	86.9	70.2	64.2
	(86.9, 88.3)	(81.9, 85.0)	(95.6, 96.8)	(85.6, 87.7)	(67.1, 72.9)	(62.1, 66.7)
<i>Dependent (channel &amp; spatial)</i>	88.1	83.9	96.5	87.7	70.8	64.5
	(87.3, 88.8)	(81.7, 85.0)	(96.1, 97.1)	(86.4, 88.6)	(67.9, 72.9)	(61.8, 66.5)
w/ <i>SGR</i> [16]	87.5	83.3	96.4	87.6	70.7	64.4
	(86.2, 88.0)	(81.6, 85.2)	(96.1, 96.7)	(86.7, 88.5)	(67.1, 72.9)	(61.1, 66.7)
w/ <i>DualGCN</i> [17]	87.8	83.9	96.8	88.0	70.9	65.0
	(86.9, 88.3)	(81.7, 85.8)	(96.4, 97.0)	(87.2, 88.8)	(67.2, 73.1)	(63.1, 67.7)
w/ <i>GloRe</i> [9]	87.9	84.1	96.9	88.3	71.2	66.1
	(86.5, 88.2)	(82.6, 86.0)	(96.5, 97.4)	(87.6, 88.9)	(68.1, 73.2)	(64.3, 67.7)
<i>Ours</i>	<b>88.8</b>	<b>85.1</b>	<b>97.7</b>	<b>91.1</b>	<b>72.7</b>	<b>67.4</b>
<i>(channel &amp; spatial) + boundary</i>	(88.1, 89.4)	(83.3, 86.8)	(97.6, 97.8)	(90.2, 92.0)	(70.1, 75.4)	(65.7, 70.1)

**Graph Convolution.** In this section, we evaluate the effectiveness of the proposed graph convolution operation. Firstly, we employ the classic graph convolution [10] to reason the correlations between regions. Then we explore the input-dependent graph convolutions in terms of channel attention (*channel*) and spatial attention (*spatial*) mechanism, respectively and simultaneously (*channel and spatial*). Additionally, we adopt three more potent *GRMs* to show the superiority of our proposed *BI-GConv*. In detail, we apply the *SGR* [16], *DualGCN* [17], and *GloRe* module [9] respectively, where the *SGR* module exploits knowledge graph mechanism; *DualGCN* explores the coordinate space and feature space graph convolution; and *GloRe* utilizes projection and re-projection mechanism to reason the semantics between different regions. These methods achieved state-of-the-art performance on different segmentation tasks, however, they all belong to the data-independent *Laplacian* based graph convolution. Tab. 3 shows that our model achieves more accurate and reliable results than [10] and outperforms the *SGR*, *DualGCN*, and *GloRe* by 1.9 %, 1.5 % and 1.3 % in terms of mean *Dice* on the two test datasets.

**Model Components.** We evaluate the effectiveness of each component of our proposed model. Firstly, we remove the *BSM* and the *GRM*; we refer to the rest of the structure as the Baseline model. Then we add *BSM* (w/ *BSM*) and single layer *BI-GConv* (w/ *BI-GConv*,  $N = 1$ ) to evaluate each component’s effectiveness gradually. Note that, in order to eliminate

Table 4: Ablation study on different graph convolutions. The performance is reported as *Dice* (%) and *BloU* (%). 95% confidence intervals are presented in the brackets, respectively.

Methods	OC		OD		Polyps	
	<i>Dice</i> (%) $\uparrow$	<i>BloU</i> (%) $\uparrow$	<i>Dice</i> (%) $\uparrow$	<i>BloU</i> (%) $\uparrow$	<i>Dice</i> (%) $\uparrow$	<i>BloU</i> (%) $\uparrow$
<i>Baseline</i>	85.1	80.0	95.5	86.3	69.1	63.4
	(84.0, 86.3)	(78.1, 81.2)	(95.0, 96.0)	(85.8, 86.7)	(66.9, 71.5)	(61.1, 65.7)
<i>w/ BSM</i>	85.8	81.5	96.1	87.7	70.3	64.1
	(84.5, 86.3)	(80.2, 82.2)	(95.4, 96.7)	(87.2, 88.3)	(69.0, 72.1)	(62.0, 65.7)
<i>w/ BI-GConv</i>	87.9	83.8	97.0	90.2	72.1	66.7
( <i>N</i> = 1)	(85.5, 89.3)	(81.1, 85.2)	(96.6, 97.3)	(89.8, 90.6)	(70.0, 74.7)	(64.1, 68.1)
<i>Ours</i>	<b>88.8</b>	<b>85.1</b>	<b>97.7</b>	<b>91.1</b>	<b>72.7</b>	<b>67.4</b>
<i>w/ BI-GConv</i> ( <i>N</i> = 3)	(88.1, 89.4)	(83.3, 86.8)	(97.6, 97.8)	(90.2, 92.0)	(70.1, 75.4)	(65.7, 70.1)

the model size difference and maintain a similar number of parameters (e.g. 32.8 million for our model), we replace the *GRMs* with several feed-forward *CNN* blocks in other ablation models (e.g., *Baseline*, *w/ BSM*, etc.) with standard convolution layer of kernel size  $3 \times 3$ , padding 1, followed by a Batch Normalization [14] layer. Tab. 4 shows that *BSM* and single layer *BI-GConv* can improve from *Baseline* model by 1.0 % and 3.4 % via the mean *Dice* on the two test datasets.

## 4 Conclusion

In this paper, we present a graph-propagation based framework to tackle biomedical image segmentation problems. We proposed a boundary-aware input-dependent graph convolution (*BI-GConv*) to reason about the boundary-enhanced long range correlations between regions in biomedical image segmentation tasks. Our experiment results show that the proposed *GRM* can efficiently reason about the semantic region features while explicitly considering spatial boundary features on the segmentation tasks of the colonic polyps and OD and OC. We will extend the proposed model to tackle 3D biomedical image segmentation tasks to learn the graph representation of volumes and object surfaces in the future.

## 5 Acknowledgements

Y. Meng and H. Zhang thank the China Science IntelliCloud Technology Co., Ltd for the studentships. We thank NVIDIA for the donation of GPU cards. This work was undertaken on Barkla, part of the High Performance Computing facilities at the University of Liverpool, Liverpool, United Kingdom.

## References

- [1] Ahmed Almazroa, Sami Alodhayb, Essameldin Osman, Eslam Ramadan, Mohammed Hummadi, Mohammed Dlaim, Muhannad Alkatee, Kaamran Raahemifar, and Vasudevan Lakshminarayanan. Retinal fundus images for glaucoma analysis: the RIGA dataset. In *Medical Imaging 2018: Imaging Informatics for Healthcare, Research, and Applications*, 2018.

- [2] Nicolas Ballas, Li Yao, Chris Pal, and Aaron C. Courville. Delving deeper into convolutional networks for learning video representations. In Yoshua Bengio and Yann LeCun, editors, *4th International Conference on Learning Representations, ICLR 2016, San Juan, Puerto Rico, May 2-4, 2016, Conference Track Proceedings*, 2016.
- [3] Jorge Bernal, F Javier Sánchez, Gloria Fernández-Esparrach, Debora Gil, Cristina Rodríguez, and Fernando Vilarinho. Wm-dova maps for accurate polyp highlighting in colonoscopy: Validation vs. saliency maps from physicians. *Computerized Medical Imaging and Graphics*, 2015.
- [4] Liang-Chieh Chen, George Papandreou, Iasonas Kokkinos, Kevin Murphy, and Alan L Yuille. Deeplab: Semantic image segmentation with deep convolutional nets, atrous convolution, and fully connected crfs. *IEEE Transactions on Pattern Analysis and Machine Intelligence*, 40(4):834–848, 2017.
- [5] Yunpeng Chen, Marcus Rohrbach, Zhicheng Yan, Yan Shuicheng, Jiashi Feng, and Yannis Kalantidis. Graph-based global reasoning networks. In *Proceedings of the IEEE/CVF Conference on Computer Vision and Pattern Recognition*, pages 433–442, 2019.
- [6] Bowen Cheng, Ross Girshick, Piotr Dollár, Alexander C Berg, and Alexander Kirillov. Boundary iou: Improving object-centric image segmentation evaluation. *Proceedings of the IEEE Conference on Computer Vision and Pattern Recognition*, 2021.
- [7] Michaël Defferrard, Xavier Bresson, and Pierre Vandergheynst. Convolutional neural networks on graphs with fast localized spectral filtering. In *Advances in Neural Information Processing Systems*, pages 3844–3852, 2016.
- [8] Deng-Ping Fan, Ge-Peng Ji, Tao Zhou, Geng Chen, Huazhu Fu, Jianbing Shen, and Ling Shao. Pranet: Parallel reverse attention network for polyp segmentation. In *International Conference on Medical Image Computing and Computer-Assisted Intervention*, pages 263–273. Springer, 2020.
- [9] Yuqi Fang, Cheng Chen, Yixuan Yuan, and Kai-yu Tong. Selective feature aggregation network with area-boundary constraints for polyp segmentation. In *International Conference on Medical Image Computing and Computer-Assisted Intervention*, pages 302–310. Springer, 2019.
- [10] Huazhu Fu, Jun Cheng, Yanwu Xu, Damon Wing Kee Wong, Jiang Liu, and Xiaochun Cao. Joint optic disc and cup segmentation based on multi-label deep network and polar transformation. *IEEE Transactions on Medical Imaging*, 37(7):1597–1605, 2018.
- [11] Francisco Fumero, Silvia Alayón, José L Sanchez, Jose Sigut, and M Gonzalez-Hernandez. RIM-ONE: An open retinal image database for optic nerve evaluation. In *24th International Symposium on Computer-based Medical Systems (CBMS)*, pages 1–6. IEEE, 2011.
- [12] Shanghua Gao, Ming-Ming Cheng, Kai Zhao, Xin-Yu Zhang, Ming-Hsuan Yang, and Philip HS Torr. Res2net: A new multi-scale backbone architecture. *IEEE Transactions on Pattern Analysis and Machine Intelligence*, 2019.

- [13] Kaiming He, Xiangyu Zhang, Shaoqing Ren, and Jian Sun. Deep residual learning for image recognition. In *Proceedings of the IEEE Conference on Computer Vision and Pattern Recognition*, pages 770–778, 2016.
- [14] Sergey Ioffe and Christian Szegedy. Batch normalization: Accelerating deep network training by reducing internal covariate shift. In *International conference on machine learning*, pages 448–456. PMLR, 2015.
- [15] Debesh Jha, Pia H Smedsrud, Michael A Riegler, Pål Halvorsen, Thomas de Lange, Dag Johansen, and Håvard D Johansen. Kvasir-seg: A segmented polyp dataset. In *International Conference on Multimedia Modeling*, pages 451–462. Springer, 2020.
- [16] Diederik P Kingma and Jimmy Ba. Adam: A method for stochastic optimization. *arXiv preprint arXiv:1412.6980*, 2014.
- [17] Thomas N Kipf and Max Welling. Semi-supervised classification with graph convolutional networks. *ICLR*, 2017.
- [18] Xia Li, Yibo Yang, Qijie Zhao, Tiancheng Shen, Zhouchen Lin, and Hong Liu. Spatial pyramid based graph reasoning for semantic segmentation. In *Proceedings of the IEEE/CVF Conference on Computer Vision and Pattern Recognition*, pages 8950–8959, 2020.
- [19] Yin Li and Abhinav Gupta. Beyond grids: Learning graph representations for visual recognition. In *Advances in Neural Information Processing Systems*, pages 9225–9235, 2018.
- [20] Xiaodan Liang, Zhiting Hu, Hao Zhang, Liang Lin, and Eric P Xing. Symbolic graph reasoning meets convolutions. In *Proceedings of the 32nd International Conference on Neural Information Processing Systems*, pages 1858–1868, 2018.
- [21] Yanda Meng, Wei Meng, Dongxu Gao, Yitian Zhao, Xiaoyun Yang, Xiaowei Huang, and Yalin Zheng. Regression of instance boundary by aggregated CNN and GCN. In *European Conference on Computer Vision*, pages 190–207. Springer, 2020.
- [22] Yanda Meng, Meng Wei, Dongxu Gao, Yitian Zhao, Xiaoyun Yang, Xiaowei Huang, and Yalin Zheng. Cnn-gcn aggregation enabled boundary regression for biomedical image segmentation. In *International Conference on Medical Image Computing and Computer-Assisted Intervention*, pages 352–362. Springer, 2020.
- [23] Yanda Meng, Hongrun Zhang, Yitian Zhao, Xiaoyun Yang, Yihong Qiao, J. C. McCormick Ian, Xiaowei Huang, and Yalin Zheng. Graph-based region and boundary aggregation for biomedical image segmentation. In *IEEE Transactions on Medical Imaging*, page in press, 2021.
- [24] Fausto Milletari, Nassir Navab, and Seyed-Ahmad Ahmadi. V-net: Fully convolutional neural networks for volumetric medical image segmentation. In *2016 Fourth International Conference on 3D Vision (3DV)*, pages 565–571. IEEE, 2016.
- [25] Balamurali Murugesan, Kaushik Sarveswaran, Sharath M Shankaranarayana, Keerthi Ram, Jayaraj Joseph, and Mohanasankar Sivaprakasam. Psi-net: Shape and boundary aware joint multi-task deep network for medical image segmentation. In *2019 41st*

*Annual International Conference of the IEEE Engineering in Medicine and Biology Society (EMBC)*, pages 7223–7226. IEEE, 2019.

- [26] José Ignacio Orlando, Huazhu Fu, João Barbossa Breda, Karel van Keer, Deepti R Bathula, Andrés Diaz-Pinto, Ruogu Fang, Pheng-Ann Heng, Jeyoung Kim, JoonHo Lee, et al. REFUGE challenge: A unified framework for evaluating automated methods for glaucoma assessment from fundus photographs. *Medical Image Analysis*, 59: 101570, 2020.
- [27] Olaf Ronneberger, Philipp Fischer, and Thomas Brox. U-net: Convolutional networks for biomedical image segmentation. In *International Conference on Medical Image Computing and Computer-assisted Intervention*, pages 234–241. Springer, 2015.
- [28] Juan Silva, Aymeric Histace, Olivier Romain, Xavier Dray, and Bertrand Granado. Toward embedded detection of polyps in wce images for early diagnosis of colorectal cancer. *International Journal of Computer Assisted Radiology and Surgery*, 9(2):283–293, 2014.
- [29] Jayanthi Sivaswamy, SR Krishnadas, Gopal Datt Joshi, Madhulika Jain, and A Ujjwaft Syed Tabish. Drishti-GS: Retinal image dataset for optic nerve head (ONH) segmentation. In *2014 IEEE 11th International Symposium on Biomedical Imaging (ISBI)*, pages 53–56. IEEE, 2014.
- [30] Nima Tajbakhsh, Suryakanth R Gurudu, and Jianming Liang. Automated polyp detection in colonoscopy videos using shape and context information. *IEEE Transactions on Medical Imaging*, 35(2):630–644, 2015.
- [31] Yih-Chung Tham, Xiang Li, Tien Y Wong, Harry A Quigley, Tin Aung, and Ching-Yu Cheng. Global prevalence of glaucoma and projections of glaucoma burden through 2040: a systematic review and meta-analysis. *Ophthalmology*, 121(11):2081–2090, 2014.
- [32] David Vázquez, Jorge Bernal, F Javier Sánchez, Gloria Fernández-Esparrach, Antonio M López, Adriana Romero, Michal Drozdal, and Aaron Courville. A benchmark for endoluminal scene segmentation of colonoscopy images. *Journal of Healthcare Engineering*, 2017, 2017.
- [33] Bo Wang, Wei Wei, Shuang Qiu, Shengpei Wang, Dan Li, and Huiguang He. Boundary aware u-net for retinal layers segmentation in optical coherence tomography images. *IEEE Journal of Biomedical and Health Informatics*, 2021.
- [34] Jun Wu, Kaiwei Wang, Zongjiang Shang, Jie Xu, Dayong Ding, Xirong Li, and Gang Yang. Oval shape constraint based optic disc and cup segmentation in fundus photographs. In *BMVC*, page 265, 2019.
- [35] Fisher Yu and Vladlen Koltun. Multi-scale context aggregation by dilated convolutions. In *ICLR*, 2016.
- [36] Fisher Yu, Dequan Wang, Evan Shelhamer, and Trevor Darrell. Deep layer aggregation. In *Proceedings of the IEEE Conference on Computer Vision and Pattern Recognition*, pages 2403–2412, 2018.

- [37] Li(\*) Zhang, Xiangtai(\*) Li, Anurag Arnab, Kuiyuan Yang, Yunhai Tong, and Philip HS Torr. Dual graph convolutional network for semantic segmentation. In *BMVC2019*.
- [38] Ruifei Zhang, Guanbin Li, Zhen Li, Shuguang Cui, Dahong Qian, and Yizhou Yu. Adaptive context selection for polyp segmentation. In *International Conference on Medical Image Computing and Computer-Assisted Intervention*, pages 253–262. Springer, 2020.
- [39] Zhijie Zhang, Huazhu Fu, Hang Dai, Jianbing Shen, Yanwei Pang, and Ling Shao. Etnet: A generic edge-attention guidance network for medical image segmentation. In *International Conference on Medical Image Computing and Computer-Assisted Intervention*, pages 442–450. Springer, 2019.
- [40] Zhuo Zhang, Feng Shou Yin, Jiang Liu, Wing Kee Wong, Ngan Meng Tan, Beng Hai Lee, Jun Cheng, and Tien Yin Wong. ORIGA-light: An online retinal fundus image database for glaucoma analysis and research. In *2010 Annual International Conference of the IEEE Engineering in Medicine and Biology*, pages 3065–3068. IEEE, 2010.
- [41] Zongwei Zhou, Md Mahfuzur Rahman Siddiquee, Nima Tajbakhsh, and Jianming Liang. Unet++: A nested u-net architecture for medical image segmentation. In *Deep Learning in Medical Image Analysis and Multimodal Learning for Clinical Decision Support*, pages 3–11. Springer, 2018.